LA-UR-18-29702
Approved for public release; distribution is unlimited.

Title: Nanoindentation Analysis of Ion Irradiated FeCrAl C26M

Author(s): Gigax, Jonathan Gregory
Aydogan, Eda
Chancey, Matthew Ryan
Wang, Yongqiang
Li, Nan

Intended for: Report

Issued: 2018-10-12

Nanoindentation Analysis of Ion Irradiated FeCrAl C26M

Fuel Cycle Research & Development

Prepared for
U.S. Department of Energy
Advanced Fuels Campaign

Jonathan G. Gigax
Eda Aydogan
Matthew Chancey
Yongqiang Wang
Nan Li

09/24/18
FCRD-FUEL-2014-000xxx

SUMMARY

The present report summarizes the irradiation hardening behavior of two FeCrAl alloys, C26M and B126Y, irradiated up to a damage level of 16 dpa. Nanoindentation values were averaged between a depth of 100 and 200 nm in order to capture the irradiated region only. At the highest damage level, C26M was measured to harden by 1.62 GPa with little change in the modulus. B126Y showed a change in hardness of up to 2.52 GPa, reaching a similar hardness to the C26M. To more accurately compare with the unirradiated material where the influence of indentation size effects may operate more strongly, the Nix-Gao model was used to calculate the hardness at infinite depth, H_0, and the length scale term, h*. The change in hardness with this model was found to be lower for both C26M and B126Y. The length scale term decreased with increasing dose up to 4 dpa and then deviated from expectation with a significant increase at 16 dpa for both specimens. Spherical nanoindentation was performed on all specimens. A 5 μm tip was used to ensure the yield point occurred in the irradiated region. While the results from this testing are not as conclusive at doses less than 4 dpa, the nanoindentation yield strength showed similar trends with the nanoindentation hardness data.

TABLE OF CONTENTS

FIGURES

TABLES

Intentionally Blank

1. Introduction

Among several candidates for "accident tolerant" fuel cladding, FeCrAl alloys are among the top choices due to their superior high temperature oxidation resistance, aqueous corrosion resistance, low radiation-induced swelling, and tolerance to loss-of-coolant accident conditions [1-4]. It is important to note that despite their higher neutron absorption cross-section compared to zirconium-based alloys, their mechanical and chemical stability over a range of environment make this alloy and attractive candidate to others (i.e. SiC-based cladding). The ongoing work led by Oak Ridge National Lab has targeted an optimized FeCrAl alloy for tube processing and implementation in light water reactors [5]. Recent testing and evaluation has led to a down selected alloy, C26M. As part of a wider effort to evaluate the mechanical properties of this alloy after irradiation, we perform initial microstructural characterization and testing using nanoindentation techniques.

2. Materials and Methods

One FeCrAl alloy, C26M with a composition given in Table 1 was provided in tube form (Heat #17025001). Specimens were cut and sectioned to expose the area perpendicular to the tube axis. Both surfaces of the tube were ground using a SiC paper with a grit of 600. One surface of the tube was polished to a final solution of 0.04 μm silica. Another FeCrAl Alloys, B126Y (composition in Table 1), was selected for comparison and prepared in a similar manner as the C26M.

Table 1. Chemical compositions of FeCrAl C26M and B126Y.

Alloy ID	Fe	Cr	Al	Y	Mo	Si	Nb	C	S	O	N
C26M	Bal.	11.87	6.2	0.030	1.98	0.2	-	<0.01	<0.005	-	-
B126Y	Bal.	12.0	6.0	0.05	-	-	-	-	-	-	-

Heavy ion irradiation of the polished tubes was performed using a 3 MV NEC Pelletron at the Ion Beam and Materials Lab (IBML) at Los Alamos National Lab. The specimens were irradiated with 5 MeV Fe^{2+} ions at a temperature of 300 C. The damage levels were calculated using the Kinchin-Pease option in SRIM with a displacement energy of 40 eV [6,7]. Damage levels were averaged in the depth range of 200-800 nm and specimens irradiated to 1, 4, and 16 dpa, corresponding to 5, 10, and 40 peak dpa.

Nanoindentation of the samples was performed on a Keysight G200 nanoindenter. The indentation used a diamond Berkovich tip and a spherical tip with a radius of 5 μm (modulus of 1130 GPa and Poisson's ratio of 0.07) in a continuous stiffness measurement mode with a tip frequency of 45 Hz and 2 nm displacement. Hardness and modulus measurements were determined using the Oliver-Pharr method [9]. A 4x4 array of indents spaced 50 μm was used for each specimen in order to sample the irradiated area across multiple grains. The hardness of each specimen was averaged over a depth of 100-200 nm. The choice of depth is due to the size of the plastic zone under the tip. In unirradiated materials, this size is ~4-10 times (larger for softer materials) the penetration depth [10]. Hardie *et al.* found that, in irradiated materials, the plastic zone was closer to ~4 the penetration depth [10]. Based on the study, our choice of averaging hardness between a depth of 100-200 nm falls cleanly in the irradiated region and excludes depths with larger amounts of injected interstitials. The indentation size effect (ISE), which results in higher hardness at shallower depths, operates on the hardness measured in this region [11-14]. In order to obtain hardness values that are more representative of deeper indents, the Nix-Gao model was used to estimate the hardness at an infinite depth, H_o, and a length scale term, h^*, from hardness, H, and displacement, h, data between 100-200 nm according to Eqn. (1).

$$\frac{H}{H_o} = \sqrt{1 + \frac{h^*}{h}} \quad (1)$$

3. Results and Discussion

3.1 Nanoindentation

Figure 1 provides typical nanoindentation hardness and modulus curves for the unirradiated sample, and samples irradiated to 1, 4, and 16 dpa as a function of indenter depth into the FeCrAl C26M alloy. All samples exhibit relatively flat profile for the modulus as a function of depth, with an average modulus between 245 GPa and 270 GPa. However, it is clear from Fig. 1b that the hardness exhibits a large gradient at shallower depths, notably in the depth range of interest. This size effect presents a concern when comparing hardness of an unirradiated microstructure with potentially fewer dislocation sources than irradiated ones at these depth intervals. Analysis of the hardness using the Nix-Gao model is addressed in the next section. Table 2 and 3 summarizes the hardness and moduli values of the unirradiated and irradiated specimens of the C26M and B126Y, respectively.

Figure 2 provides a comparison of the hardness and modulus of the unirradiated and irradiated specimens for both the C26M and B126Y. While the moduli of the specimens show little variation with dose, the hardness exhibits a monotonic increase with increasing damage level. It is clear that the C26M shows a lesser amount of hardening with increasing dose compared to the B126Y. While it is not necessarily rigorous proof of a hardness saturation, the trend suggests that irradiation to higher damage levels may not result in any significant increases in hardness. The differences in hardness change can be attributed to the starting microstructure of the tubes. B126Y, while also a tube, showed little in-grain misorientation from EBSD scans, suggesting that heat treatments had been performed. However, the C26M showed a microstructure that had not been heat treated, thus started with some amount of cold-work. This resulted in a lower hardness compared to the C26M before irradiation. It is worth noting both the C26M and B126Y reached similar hardness values at 16 dpa.

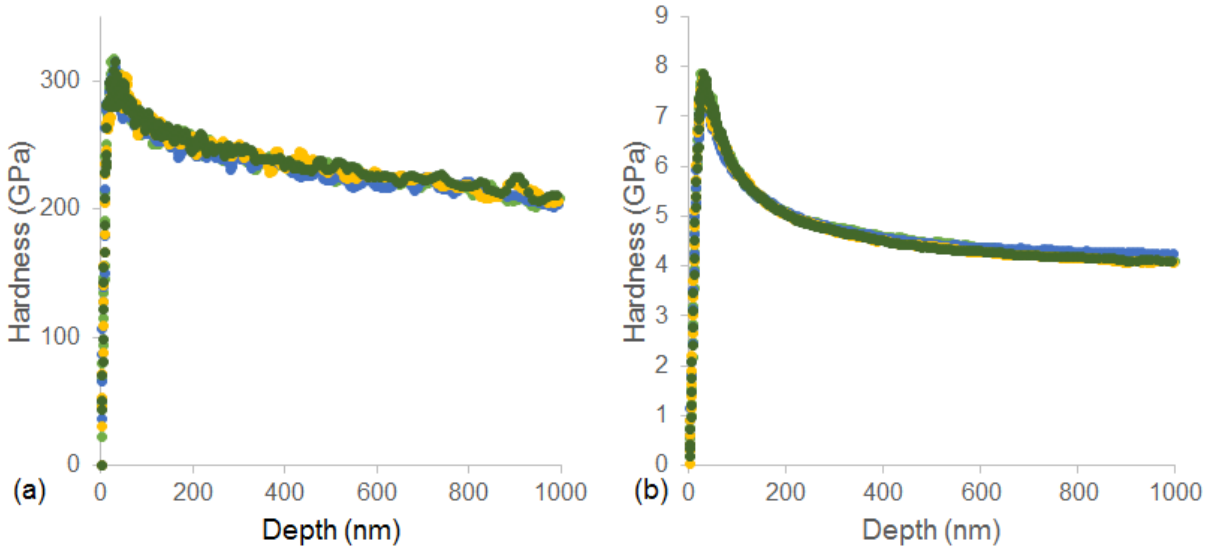

Figure 1. Representative indentation (a) modulus) and (b) hardness data for unirradiated C26M.

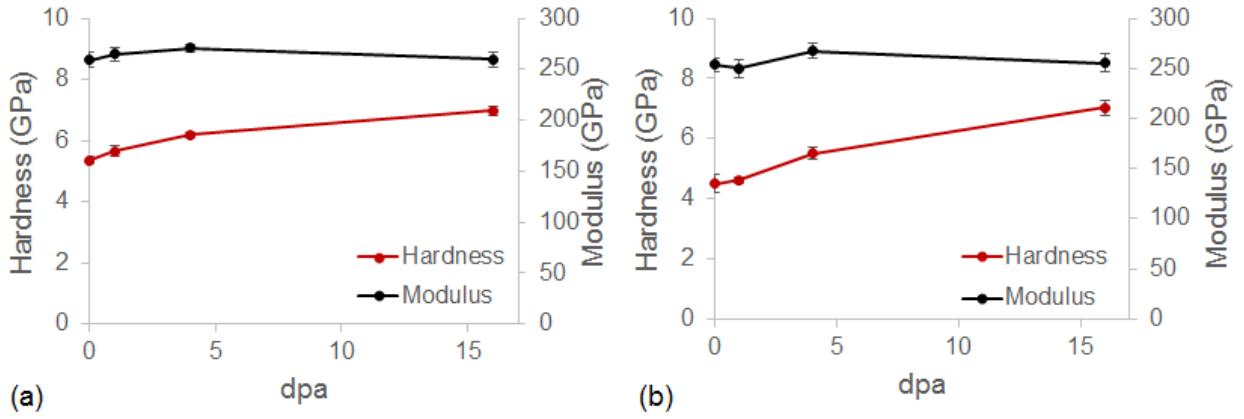

Figure 2. Hardness and modulus of unirradiated (a) C26M and (b) B126Y, and the specimens irradiated to 1, 4, and 16 dpa. Values are averaged between a depth of 100 and 200 nm.

Table 2. Summary of nanoindentation measurements for C26M. The average for each test is taken over 100-200 nm displacement. Sample averages come from 16-25 tests spaced in various grains.

dpa	Modulus (GPa)	Hardness (GPa)	ΔH
0	258.9 ± 7.3	5.36 ± 0.12	0 ± 0
1	265 ± 6.6	5.66 ± 0.17	0.3 ± 0.21
4	270.7 ± 3.3	6.18 ± 0.11	0.82 ± 0.16
16	259.7 ± 7.3	6.98 ± 0.15	1.62 ± 0.19

Table 3. Summary of nanoindentation measurements for B126Y. The average for each test is taken over 100-200 nm displacement. Sample averages come from 16-25 tests spaced in various grains.

dpa	Modulus (GPa)	Hardness (GPa)	ΔH
0	253.9 ± 6.9	4.5 ± 0.31	0 ± 0
1	250.1 ± 8.7	4.62 ± 0.11	0.12 ± 0.33
4	267.2 ± 7.6	5.49 ± 0.2	0.99 ± 0.37
16	255.7 ± 8.9	7.02 ± 0.25	2.52 ± 0.40

3.2 Consideration of Nanoindentation Size Effect

Figure 3 shows the hardness at infinite depth, H_0, and the length scale term, h*, determined using the Nix-Gao model and linear regression of the hardness-displacement data from a depth range between 100 and 200 nm for both the C26M and B126Y. Tables 4 and 5 provide a summary of the Nix-Gao model values for the C26M and B126Y, respectively. The hardness data possesses the same trend as in Fig. 2, albeit with a smaller overall change in hardness. That is, the differences in hardness between the irradiated specimens is less than that calculated by nanoindentation results only. This indicates the impact that differences in microstructural defects have on the size effects that influence hardness in the unirradiated and irradiated specimens at these shallower penetration depths.

The length scale term shows a dramatic decrease from the unirradiated specimen to 4 dpa. The decrease in the h* value indicates the reduction of a size effect, or the length beyond which more bulk-like properties are expected to be measured with nanoindentation. This reduction points to an increase in

dislocation sources and/or reduction in the geometrically necessary dislocations needed for deformation in the strain region under the indenter tip at shallow depths. The apparent increase in the h* value at 16 dpa cannot be easily explained. Calculation of both H_0 and h* are performed by a linear fit of the hardness data as a function of depth. While the data is sensitive to noise and microstructural heterogeneities, averaging over several sets should limit the influence of these issues. Furthermore, the depth range for the linear fits was adjusted to larger values (50-200 nm) without a significant change in the observed trend for h*. Additional microstructural investigation is needed in order to understand if any significant differences in defect structure or morphology are present between specimens irradiated at low damage levels and ones irradiated at higher damage levels.

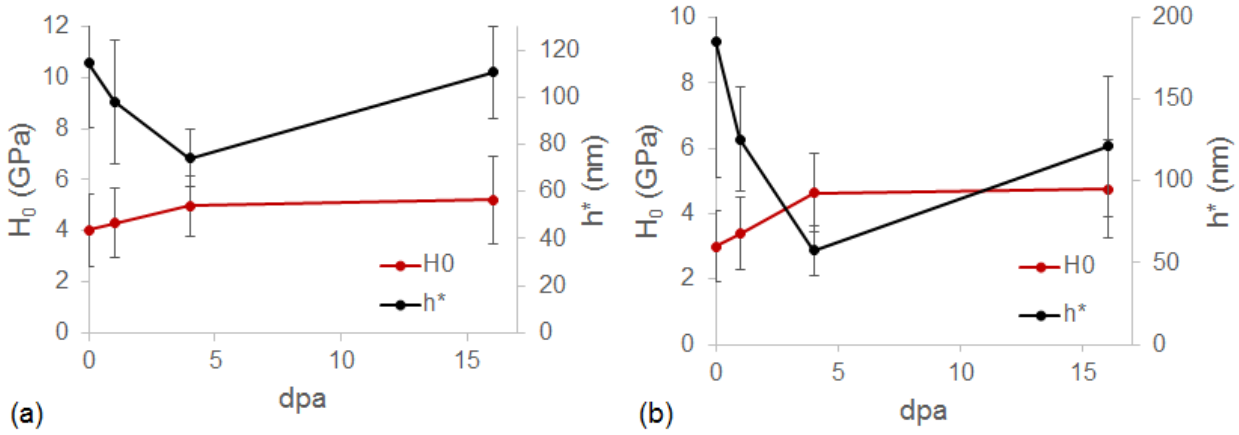

Figure 3. Hardness at infinite depth, H_0, and the length scale term, h*, from the Nix-Gao model for unirradiated and irradiated (a) C26M and (b) B126Y, respectively.

Table 4. Summary of Nix-Gao model parameters and change in hardness for the C26M.

Dose (dpa)	H0 (GPa)	h* (nm)	ΔH_0
0	4.02 ± 1.42	114.4 ± 27.1	0 ± 0
1	4.30 ± 1.35	98.1 ± 26.5	0.29 ± 1.96
4	4.97 ± 1.17	74.1 ± 12.1	0.96 ± 1.84
16	5.21 ± 1.71	110.6 ± 19.6	1.19 ± 2.22

Table 5. Summary of Nix-Gao model parameters and change in hardness for the B126Y.

Dose (dpa)	H0 (GPa)	h* (nm)	ΔH_0
0	3.0 ± 1.10	185.5 ± 83.8	0 ± 0
1	3.38 ± 1.11	125.5 ± 32.0	0.38 ± 1.56
4	4.63 ± 1.20	57.7 ± 15.2	1.63 ± 1.63
16	4.76 ± 1.50	121.2 ± 43.1	1.76 ± 1.86

3.3 Spherical Nanoindentation

Spherical nanoindentation offers the possibility of gaining additional insights to the changes in the mechanical properties of the irradiated specimens by probing more confined volumes of material compared to a Berkovich tip. However, it is important select the proper tip when performing the indentation to maximize the information obtained from the irradiated volume or, at the very least, ensure that the nanoindentation yield point is within the irradiated region. While smaller tip sizes may appear to

provide the best solution, they are also more sensitive to surface features and roughness as well as displaying more pop-in behavior due to the smaller volume probed. As a balance between the two concerns, we used a 5 μm radius tip for nanoindentation with a similar loading configuration as the Berkovich indentation. Fig. 4 provides a comparison of the nanoindentation stress-strain curves for the C26M and B126Y at 0, 1, 4, and 16 dpa, respectively, in grains with an orientation near (111). Table 6 provides a summary of the spherical nanoindenation data for C26M and B126Y.

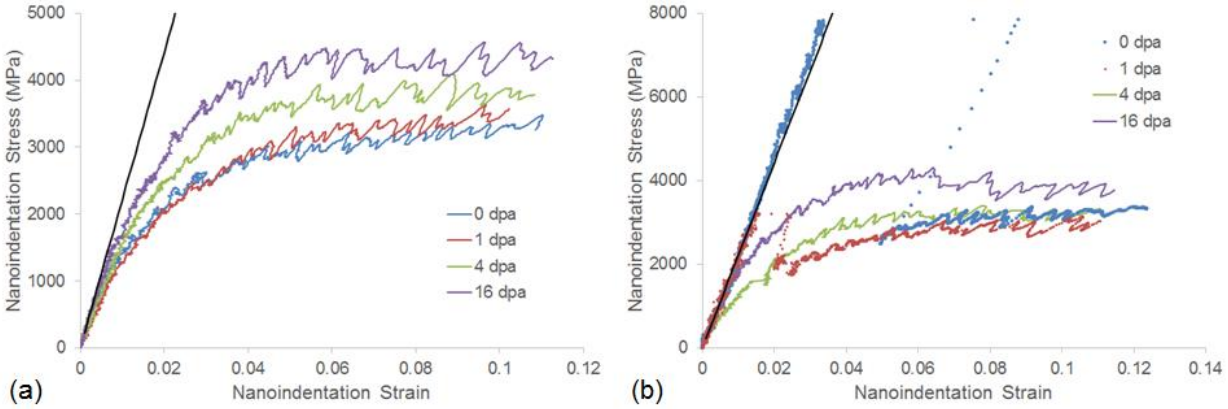

Figure 4. Spherical nanoindentation stress-strain curves of the unirradiated and irradiated (a) C26M and (b) B126Y taken from grains near the (111) orientation. A straight line with the slope equal to the modulus is provided in each plot as a solid black line.

For spherical nanoindentation, the stress field under the tip extends to a depth of ~2.4*a*, where *a* is the contact radius of the tip with the surface of the sample. At a nanoindentation strain value of 0.02, the contact radius of the indenter is 300-450 nm with an indentation zone of 700-1100 nm, near the end of ion range. The yield point occurs at a contact radius of 100-150 nm (300-450 nm indentation zone), within the irradiated region. For the C26M, the nanoindentation stress-strain curves show an increasing yield strength with increasing dose. Due to the relatively low defect density in the B126Y, the unirradiated and 1 dpa specimens tend to show more pop-ins in the stress-strain curve than those at higher doses. This complicates analysis as linear regression must be used to estimate the yield strength and typically overestimates the yield strength. However, with increasing dose, the pop-ins largely disappear and closely resemble the C26M nanoindentation stress-strain curves.

Table 6. Summary of the spherical nanoindentation analysis for C26M and B126Y.

	C26M		B126Y	
dpa	Modulus (GPa)	Nanoindentation Yield Strength (MPa)	Modulus (GPa)	Nanoindentation Yield Strength (GPa)
0	217.4 ± 6.5	805.0 ± 251.7	221.7 ± 9.28	818.7 ± 259.1
1	217.0 ± 5.7	992.7 ± 390.3	215.6 ± 5.55	837.3 ± 169.9
4	220.5 ± 4.8	1184.6 ± 355.3	222.8 ± 6.42	895.3 ± 188.9
16	219.2 ± 3.2	2012.8 ± 388.5	220.8 ± 3.90	1969.7 ± 326.1

From Table 6, it can be seen that the calculated modulus for both C26M and B126Y are similar. Statistically, the nanoindentation yield strength of the specimens does not increase significantly until 4 dpa and nearly doubling at 16 dpa. It is also worth noting that the nanoindentation yield strength for C26M and B126Y are similar at 16 dpa, in agreement with the hardness data at this damage level.

4. Conclusions and Future Work

The current work highlights the recent findings on the nanoindentation behavior of a down-selected FeCrAl alloy, C26M, and another alloy, B126Y. Hardness values were observed to increase monotonically with increasing damage level for both specimens, reaching similar values at the high dose of 16 dpa. The change in hardness in the C26M decreased with increasing damage level, indicating the possibility of saturation in hardness, but that not yet occurred. The Nix-Gao model was used to calculate the hardness at infinite depth and length scale term to provide a better comparison of the irradiated samples to the unirradiated at shallow depths where the ISE operates. In the C26M, the trend of H_0 closely matched that of the nanoindentation hardness. H_0 for B126Y did deviate slightly as change in hardness at the higher doses was more significant than that observed for H_0. However, the length scale term, which is expected to decrease with increasing defect density, was observed to deviate from expectation significantly at 16 dpa for both specimens.

Spherical nanoindentation testing on both specimens revealed similarities with the nanoindentation hardness data. First, the moduli of both specimens at all doses were similar. Second, the nanoindentation yield strength increased monotonically with increasing dose, although significant changes were only observed at doses higher than 4 dpa. The nanoindentation yield strength at 16 dpa for C26M and B126Y were similar in value, and in agreement with the hardness data obtained from Berkovich indentation.

Ongoing work to produce micropillars in the irradiated tubing is underway. Micropillar compression, unlike indentation, produces a uniaxial stress field that can provide insights into the compressive yield and hardening behavior. Due to the limited volume arising from heavy ion irradiation, micropillars will be made with a width/diameter ~1 μm. It is expected that size effects will be present in these pillars. Microstructural analysis of the irradiated B126Y will also be performed to assist in comparisons with the C26M and allow for calculations of the expected hardness/yield strength changes to evaluate the applicability of indentation techniques to mechanical testing of ion irradiated materials.

5. References

[1] R.B. Rebak, K.A. Terrani, W.P. Gassmann, J.B. Williams, K.L. Ledford. Improving Nuclear Power Plant Safety with FeCrAl Alloy Fuel Cladding, MRS Advances (2017) 1-8.
[2] Y. Yamamoto, B.A. Pint, K.A. Terrani, K.G. Field, Y. Yang, L.L. Snead. Development and property evaluation of nuclear grade wrought FeCrAl fuel cladding for light water reactors, J Nucl Mater 467, Part 2 (2015) 703-716.
[3] K.G. Field, M.N. Gussev, Y. Yamamoto, L.L. Snead. Deformation behavior of laser welds in high temperature oxidation resistant Fe–Cr–Al alloys for fuel cladding applications, J Nucl Mater 454 (2014) 352-358.
[4] S.J. Zinkle, K.A. Terrani, L.L. Snead. Motivation for utilizing new high-performance advanced materials in nuclear energy systems, Current Opinion in Solid State and Materials Science 20 (2016) 401-410.
[5] Y. Yamamoto, Z. Sun, B.A. Pint, K.A. Terrani. Optimized Gen-II FeCrAl cladding production in large quantity for campaign testing. Oak Ridge: Oak Ridge National Laboratory, 2016.
[6] J.F. Ziegler. SRIM-2003, Nuclear Instruments and Methods in Physics Research Section B: Beam Interactions with Materials and Atoms 219–220 (2004) 1027-1036.
[7] R.E. Stoller, M.B. Toloczko, G.S. Was, A.G. Certain, S. Dwaraknath, F.A. Garner. On the use of SRIM for computing radiation damage exposure, Nuclear Instruments and Methods in Physics Research Section B: Beam Interactions with Materials and Atoms 310 (2013) 75-80.
[8] E. Aydogan, J.S. Weaver, Y. Wang, S.A. Maloy, N.A. Mara. Ion Irradiation and Microstructural Characterization of Optimized FeCrAl Tubes. Los Alamos National Laboratory, 2017.
[9] W.C. Oliver, G.M. Pharr. Measurement of hardness and elastic modulus by instrumented indentation: Advances in understanding and refinements to methodology, J Mater Res 19 (2004) 3-20.

[10] C.D. Hardie, S.G. Roberts, A.J. Bushby. Understanding the effects of ion irradiation using nanoindentation techniques, J Nucl Mater 462 (2015) 391-401.
[11] W.D. Nix, H.J. Gao. Indentation size effects in crystalline materials: A law for strain gradient plasticity, Journal of the Mechanics and Physics of Solids 46 (1998) 411-425.
[12] Y. Huang, F. Zhang, K.C. Hwang, W.D. Nix, G.M. Pharr, G. Feng. A model of size effects in nano-indentation, Journal of the Mechanics and Physics of Solids 54 (2006) 1668-1686.
[13] J.G. Swadener, E.P. George, G.M. Pharr. The correlation of the indentation size effect measured with indenters of various shapes, Journal of the Mechanics and Physics of Solids 50 (2002) 681-694.
[14] G.M. Pharr, J.H. Strader, W.C. Oliver. Critical issues in making small-depth mechanical property measurements by nanoindentation with continuous stiffness measurement, J Mater Res 24 (2009) 653-666.